A Technique to Predict Clefting of Lobed Super-Pressure Balloons

Journal:	*11th AIAA ATIO Conference, AIAA Centennial of Naval Aviation Forum*
Manuscript ID:	Draft
luMeetingID:	2511
Date Submitted by the Author:	n/a
Contact Author:	Pellegrino, Sergio; California Institute of Technology

A Technique to Predict Clefting of Lobed Super-Pressure Balloons

X. Deng* and S. Pellegrino†

California Institute of Technology, Pasadena, California 91125

Lobed super-pressure balloons have shown a tendency to deploy into unexpected asymmetric shapes, hence their design has to strike a balance between the lower stresses achieved by increasing lobing and the risk of incomplete deployment. This paper proposes a computational clefting test that can be applied to any given balloon design. The test consists in setting up the balloon in its symmetrically inflated configuration, then breaking the symmetry of this shape by artificially introducing a clefting imperfection, and finally determining the equilibrium shape of the balloon. Wrinkling of the balloon film and frictionless contact are included in the computation. The clefting test is applied successfully to three 27 m diameter super-pressure balloons that have been tested indoors by NASA, of which one had remained clefted when it was inflated and the other two had deployed completely.

I. Introduction

The lobed shape of super-pressure balloons, chosen for its structural efficiency, has led to complications during deployment: several balloons did not deploy into the expected, cyclically symmetrical equilibrium configuration, but instead settled into unexpected asymmetric shapes. Incomplete deployment occurred during the 555NT test flight in Sweden and a characteristic S-cleft, i.e. a single non-meridional cleft spanning from top to bottom of the balloon and involving several lobes, was observed, see Figure 1.

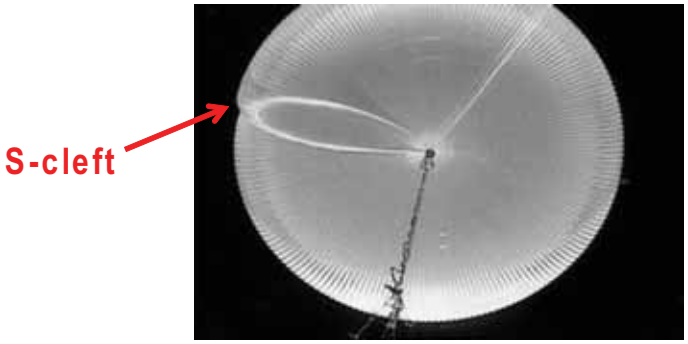

Figure 1. S-cleft observed during Sweden flight 555NT (courtesy of NASA BPO).

Extensive clefting is a regular feature of partially inflated balloons during launch and ascent and yet some balloons remain clefted when they are fully pressurized and others don't. Highly lobed balloon designs achieve lower film stress and yet are more prone to clefting. The purpose of this paper is to establish a computational clefting test that can be applied to any given balloon design. The test consists in setting up the balloon in its symmetrically inflated configuration, then breaking the symmetry of this shape by artificially introducing a clefting imperfection, and finally determining the equilibrium shape of the balloon.

*PhD Candidate, Graduate Aerospace Laboratories, 1200 East California Boulevard.

†Joyce and Kent Kresa Professor of Aeronautics and Professor of Civil Engineering, Graduate Aerospace Laboratories, 1200 E. California Blvd. MC 301-46. AIAA Fellow. sergiop@caltech.edu

The clefting imperfection is computed by shifting the constraint at the bottom of the balloon and removing the pressure in the bottom region, below the shifted constraint. Thus the equilibrium shape of the balloon becomes asymmetric and a large cleft appears. Once this disturbance has been introduced, the bottom constraint is returned to the bottom apex and a uniform pressure is applied to the whole balloon. Wrinkling and frictionless contact are included in the analysis.

A systematic set of indoor inflation experiments on one-third scale models of flight balloons were carried out in 2007 by the NASA Balloon Program Office.[1] Out of these tests we have chosen three representative ones to test the performance of our clefting test: (1) balloon # 1 with maximum bulge angle of 98.1° and maximum bulge radius of 0.284 m; (2) balloon # 4 with maximum bulge angle of 55°; (3) balloon # 5 with maximum bulge angle of 90°. In the tests balloon # 1 remained clefted, with a typical S-cleft at a pressure of 10 Pa, while the other two balloons deployed completely.

The paper is organized as follows. Section II presents a brief review of the literature on buckling, postbuckling and partially inflated shapes of balloons. Section III introduces the modeling approaches that have been selected for the present study and describes some specific ABAQUS/Explicit simulation techniques that have been developed. Section IV presents the finite element modeling details. Section V to Section VII present simulation results for the three 27 m diameter balloons that had been tested by NASA. Section VIII concludes the paper.

II. Background

Early explanations of the incomplete deployment focused on considerations of volume[2,3] or minimization of potential energy.[4–6] Pagitz and Pellegrino[7] developed a symmetry-adapted formulation of the tangent stiffness matrix and found that the critical buckling pressure p_{crit} is related to the number of (identical) lobes n by $p_{crit} = an^k$ where a and k depend on the cutting pattern of the lobes and the material properties. Xu[8] investigated the post-buckling behavior of a balloon with 64 lobes, starting from an initially symmetric configuration and using the eigenmodes of the tangent stiffness matrix as geometric perturbations. An imperfection based on the single most critical eigenmode led to a globally buckled shape whereas a more localized deformed shape was obtained by introducing an imperfection based on a combination of 10 eigenmodes. Baginski[9] analyzed the Hessian (matrix of second derivatives) of the total potential energy and found a correlation between incomplete deployment and the number of negative eigenvalues of the Hessian when the boundary constraint at the top apex are partially released. Two unstable configurations for the 230-gore 14.836 mcf design are presented in Figure 2. Note that this structure with a free top apex has only two unstable eigenmodes, with two-lobe and three-lobe symmetry. However, none of these analyses produced any deformed shapes that resembled the S-clefts that had been observed experimentally.

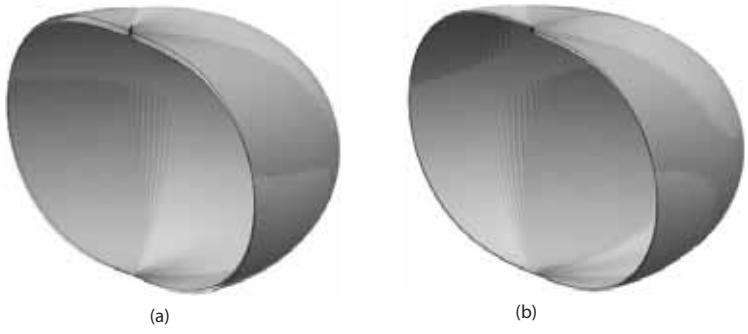

Figure 2. Asymmetric equilibrium configurations of a 230-gore 14.836 mcf balloon: (a) two-lobe symmetry (b) three-lobe symmetry (from Ref.[9]).

In recent papers,[10,11] we have attacked this problem by carrying out partial deflation and reinflation simulations that start from the cyclically symmetric inflated shape. This technique was applied to 200 lobe balloons with different lobe designs, to investigate the uniqueness of their inflated shape. It was found that balloons with flatter lobes return to their original, symmetric shape while others do not. At the end of the deflation-reinflation cycle, a clefted shape was obtained for the balloon with a high lobe angle. However, the shape of the cleft did not fully agree with the experimental observations. In addition, although this analysis

method produces detailed snapshots of the final stages of the inflation process that are useful to better understand clefting behavior, it is computationally quite onerous and hence unsuitable for the analysis of multiple balloon design configurations.

III. Modeling and Special Simulation Techniques

We use ABAQUS/Explicit (version 6.8), a general purpose finite element software to compute the dynamic response of a structure subject to time-varying loads or boundary conditions, for our clefting test. By ensuring that the loading rate is sufficiently slow, the dynamic response of the structure is sufficiently small that the response becomes effectively quasi-static. The results presented in this paper were obtained by carrying out the quickest possible simulations while ensuring that the kinetic energy is only a small fraction of the strain energy. Note, however, that a small amount of kinetic energy is required to allow large deformations of the balloon take place in a reasonable amount of time, hence introducing an excessive amount of damping may lead to inaccurate results.

Our finite element model incorporates several features that are specific to the analysis of balloon structures, as discussed below. This section also presents a variety of techniques that have been devised to achieve better results from the simulations.

A. Constraint Shift Method

A finite-element model of the balloon is initially defined, assuming its shape to be n-fold symmetric. A good initial approximation of this configuration[7] is provided by the isotensoid (axisymmetric surface in equilibrium under uniform pressure with zero circumferential stress[2,12,13]). Hence, we initially define the tendons to lie at the intersections of equally spaced meridional planes and the isotensoid. In Step 1 of the analysis a clefting perturbations is introduced by the following steps: (i) the balloon is constrained at a single offset point F, at a radial distance from the axis of one-third the radius at the equator; (ii) a positive lift is created by assigning the non-uniform pressure differential $\Delta p = \Delta p_D + \gamma(x - x_D)$ where D is the bottom apex point and $\gamma = \Delta\rho g$, where $\Delta\rho$ is the relative density of the balloon gas, and g is the gravity acceleration; and (iii) the symmetric equilibrium shape is destabilized by setting $\Delta p = 0$ in the bottom region Ω_1. Step 1 of our analysis consists in finding the equilibrium shape of the balloon for these conditions. In step 2 of the analysis the constraint is moved to the central point O at the bottom of the balloon and the non-zero pressure distribution Δp is applied to the whole balloon, to determine if a clefted shape is a possible equilibrium configuration for the balloon. This step is actually divided into a series of sub-steps with gradually decreasing numerical damping, until convergence to the final equilibrium shape is obtained. Intermediate results and a plot of energy components are provided in Figure 3.

B. Wrinkling and Contact

A cleft is a stable equilibrium shape that is associated with both wrinkling in the film of the balloon and contact between different parts of the balloon. A user-defined subroutine (Vumat) was used to model wrinkling in the film and thus avoid compressive stresses. A mixed wrinkling criterion based on the variable Poisson's ratio method[14,15] was adopted. Denoting the constitutive model for the membrane by $\{\sigma\} = [D]\{\varepsilon\}$, and the major and minor principal stresses respectively by σ_1, σ_2, this subroutine iteratively modifies the matrix D according to the state (wrinkled, taut or slack) of each element, as follows.

- $\sigma_2 > 0$: the membrane is *taut*, hence

$$D_t = \frac{E}{1-\nu^2}\begin{bmatrix} 1 & \nu & 0 \\ \nu & 1 & 0 \\ 0 & 0 & (1-\nu)/2 \end{bmatrix} \tag{1}$$

- $\sigma_2 \leq 0$ and $\varepsilon_1 > 0$: the membrane is *wrinkled*, hence

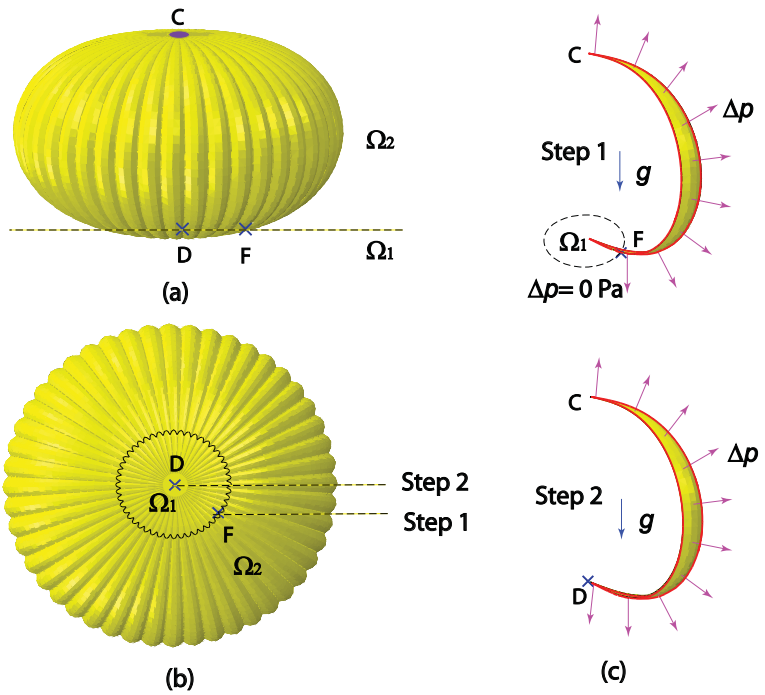

Figure 3. Schematic of loading and boundary conditions: (a) side view; (b) bottom view; (c) pressure Δp on one lobe.

$$D_w = \frac{E}{4}\begin{bmatrix} 2(1+P) & 0 & Q \\ 0 & 2(1-P) & Q \\ Q & Q & 1 \end{bmatrix} \tag{2}$$

where $P = (\epsilon_x - \epsilon_y)/(\epsilon_1 - \epsilon_2)$ and $Q = \gamma_{xy}/(\epsilon_1 - \epsilon_2)$

- $\varepsilon_1 \leq 0$ and $\sigma_2 < 0$: the membrane is *slack* and hence $D_s = 0$

It is also essential to model contact, to prevent the penetration of any parts of the balloon through other parts. ABAQUS/Explicit can handle contact in two different ways, contact pairs and general contact. The latter was used: general contact was defined for the surface of the balloon interacting with itself, using the option "*Contact Inclusions". Unlike ABAQUS/Standard, Explicit is able to handle multiple contact surfaces without a significant overhead.

C. Time Stepping

The central difference operator used in ABAQUS/Explicit is only conditionally stable and a conservative estimate of the stable time increment is calculated from

$$\Delta t_{stable} \leq \frac{L_{min}}{C_d}(\sqrt{1+\varepsilon_{max}^2} - \varepsilon_{max}) \tag{3}$$

where L_{min} is the smallest element length anywhere in the mesh, ε_{max} is the fraction of critical damping in the mode with the highest frequency and C_d is the dilatational wave speed. The dilatational wave speed C_d can be expressed for a linear elastic material as

$$C_d = \sqrt{\frac{E(1-\nu)}{\rho(1+\nu)(1-2\nu)}} \tag{4}$$

where ν is the Poisson's ratio, E is the Young's modulus and ρ is the material density. ABAQUS/Explicit will automatically calculate the time increments using Eq. 3. Hence when L_{min} becomes small and damping is increased, smaller time increments will result, which may significantly extend the time required to carry out a simulation.

D. Initial Mesh

The finite element simulation starts from a cyclically symmetric balloon subject to uniform pressure, hence the applied pressure should not be too high otherwise the balloon will buckle into a 3-up-3-down or 4-up-4-down mode.[7]

To achieve a symmetric shape, the initial mesh for the gore cutting pattern should be symmetric about the x and z axes and all lobes should be identical. Different initial meshes can be considered, see Figure 4. In this study, scheme (b) was chosen for the triangular mesh because the triangles form a tessellation of rhombuses which distributes the stiffness of the elements more uniformly. In addition, care is needed in defining the edges of the cutting pattern accurately, because even small amounts of extra material near the apex region can substantially decrease the critical buckling pressure of the balloon.

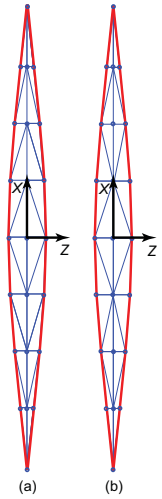

Figure 4. Schemes of initial triangular mesh.

E. Large Distortion of Elements

It was found that the simulations tend to slow down when the initial axi-symmetric configuration was perturbed by clefting, because the time increment used in the dynamic integration became very small at this stage. The main reason was that the quality of the mesh deteriorates in heavily wrinkled regions, which can be explained as follows. Consider the element ABC shown in Figure 5, AB and BC are aligned with the hoop and meridional directions respectively. During the computation of the clefting imperfection, meridional wrinkles will form when the hoop stress becomes zero, then AB is allowed to contract, whereas the meridional tension keeps the length of BC essentially unchanged.

As a measure of the distortion of the element, consider the aspect ratio AR, defined as the ratio between the radius of the circumcircle of the element and the radius of the inscribed circle

$$AR = \frac{r_c}{r_i} \tag{5}$$

The best value of AR is 0.5, for the case of an equilateral triangle, and the worst is infinite, for a triangle so elongated that one edge length is zero. In general, larger values of AR indicate greater distortion from an optimal mesh, as shown schematically in Figure 5.

Excessive dynamic behavior during the simulation will compound this effect as large dynamic distortions of the elements may occur. Numerical damping is used to reduce excessive oscillation, through the linear

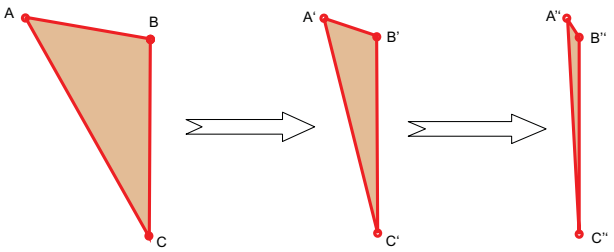

Figure 5. Deterioration of element aspect ratio during a simulation.

viscosity coefficient (option "*Bulk Viscosity" in ABAQUS/Explicit). According to Equation 3, the stable time increment, Δt_{stable}, is decreased by increasing the viscosity coefficient, ε_{max}, .

Elements with acceptable values of AR may become increasingly distorted during the course of the simulation. If a wrinkled element has $AR > 10$ it is simply deleted. In subsequent steps, the AR of elements that have been deleted is checked and any elements whose AR has become smaller than 6.7 are restored.

Note that when element deletion is implemented, a new model with the updated geometry is constructed and the stresses are set to zero everywhere. By updating the initial mesh geometry in the reference configuration, the next analysis step will calculate the correct shape and corresponding stress distribution, for the current pressure. The dynamic disturbance introduced by this procedure is typically quite small, because the current configuration is largely unchanged, only the element mesh has been altered.

IV. Finite Element Model

A simple description of the geometry can be obtained by placing the tendons on the surface of an isotensoid and by designing a cutting pattern such that the unstressed lobes span straight across the tendons. The following relationships[16] exist between the equatorial radius of the isotensoid, R_{eq}, and its height, X_h, volume, V, and meridional arc length, S_0:

$$X_h = 2 \times 0.5991 \times R_{eq} \tag{6}$$

$$V = 2.7458 \times R_{eq}^3 \tag{7}$$

$$S_0 = 2.6221 \times R_{eq} \tag{8}$$

The geometric parameters of the three test balloons are presented in Table 1. For large values of the local meridional radius and large lobe number, the lobe shape can be described by a circular arc. As shown in Figure 6(b), R is the isotensoid radius, and r is the bulge radius. θ measures the subtended angle between adjacent meridians while α measures the bulge angle. Note that for flat facet lobes, $R = r$ and $\theta = \alpha$, but for highly lobed balloons, the above four parameters are related by

$$r \sin\frac{\alpha}{2} = R \sin\frac{\theta}{2} \tag{9}$$

For the case of 200 lobes $\theta = 360/200 = 1.8°$. The nodal coordinates on the 3D balloon surface are obtained by measuring the width of the flat cutting pattern and then fitting a circular arc to it. Finally the lobe is copied and rotated $n - 1$ times to form a periodically symmetric surface, see Figure 6(a). The mesh for each lobe consists of a uniform subdivision into 68 elements between the two end fittings in the x-direction, with up to 4 triangular elements across the width.

The balloon film is made of Linear Low Density Polyethylene (LLDPE), which is a visco-elastic material, whose behavior depends on stress σ, temperature T and loading time t. Rand developed a nonlinear viscoelastic constitutive model for this film material based on Schapery's theory and subsequently we introduced an approximate pseudo-elastic constitutive model that allows for visco-elastic effects in a simplified way.[17] The anisotropy of the balloon film is sufficiently weak that an isotropic wrinkling model can be assumed. Young's Modulus and Poisson's ratio are averaged between the machine direction and the transverse direction of the film.[17] In the present case we have determined that for a balloon subject to uniform pressure $\Delta p = 10$ Pa, at room temperature $T = 293$ K for $t = 1$ hour an isotropic pseudo-elastic modulus

Table 1. Geometry of super-pressure balloons

Balloon No.	1	4	5
Bulged angle	98°	55°	90°
Diameter (m)	27.25	27.50	27.46
Height (m), z_h	16.20	16.42	16.35
Gore Length (m), S_0	35.45	35.93	35.78
Volume (m^3), V	6842	7092	7021
Radius of apex plate (m)	0.406	0.406	0.406

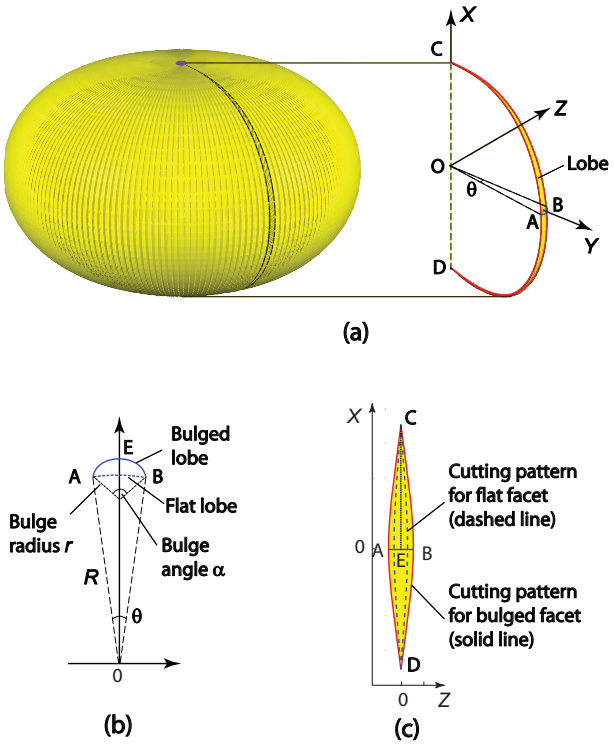

Figure 6. Schematic of 200-lobe balloon: (a) Initial geometry of the whole balloon (3D); (b) Equatorial cross section of one lobe; (c) Flat cutting pattern (2D).

of approximately 250 MPa can be assumed. This value was used for all of the simulations presented in this paper.

The tendons are made of Braided PBO. Their properties are given in Table 2.

Table 2. Pseudo-elastic material properties

LLDPE film	
Thickness of film, (mm)	0.013
Young's Modulus, (N/mm^2)	250
Poisson's ratio, ν	0.678
Density, ρ (kg/m^3)	920
PBO tendons	
Stiffness EA, (kN)	85
Density, ρ (kg/m)	0.006

In the NASA tests the balloons were initially filled with 18.3 kg of helium at atmospheric pressure and then fully inflated by adding air. The fully inflated volume was approximately 7000 m^3 and hence the specific buoyancy due to the differential density between the air outside and the mixed helium and air inside the balloon was $\gamma = 0.162$ N/m^3.

V. Results for Balloon # 1 with 98^o Bulge Angle

Following the procedures described in Sections III and IV, in step 1 of the analysis the bottom pressure was set at $\Delta p_D = 10$ Pa and a constant gradient 0.162 Pa/m was imposed in the domain Ω_1, while in step 2, the same pressure distribution was applied over the whole domain $\Omega_1 \bigcap \Omega_2$. Gravity g= 9.8m/s^2 was also included in both steps. Step 2 was actually divided into a series of substeps with gradually decreased viscosity coefficients until the final equilibrium shape was obtained. The simulation steps are presented in Table 3.

Figure 7 shows the energy variation during the two-step simulations. The bottom pressure Δp varies smoothly from 0 Pa to 10 Pa during step 1 and then remains constant. Oscillations in the kinetic energy and viscous dissipation indicate that the simulation results during step 1 are unstable. The subsequent three substeps were restarted by constructing a new model with the updated geometry from the end of the previous substep while setting the stress to zero everywhere. The strain energy remains nearly constant while the kinetic energy is stabilized.

A detailed understanding of the deformation from the original, symmetric shape to the final clefted configuration can be obtained from the plots in Figure 8(a-c), showing the components of displacement in the cylindrical coordinate system X, r, θ. The plot of axial displacement ΔX, Figure 8(a), shows a high degree of localization near the cleft, upward by around 0.8 m (red) on the left and downward by around 0.7 m (blue) on the right. The plot of Δr, Figure 8(b), shows that the balloon has expanded radially almost everywhere: the average values of Δr are $\overline{\Delta r} = +0.018$ m over $\theta = (-180, -20)$ and $\overline{\Delta r} = +0.020$ m over $(25, 180)$ deg. The cleft involves a mostly inward displacement, with $\overline{\Delta r} = -0.907$ m over the large

Table 3. Constraint shift simulation steps for balloon # 1

Step		Loading time (s)	Viscosity coefficient
Step No.	Substep No.		
1	1	8.0	0.4
2	2	5.0	2.0
	3	5.0	1.0
	4	5.0	0.5

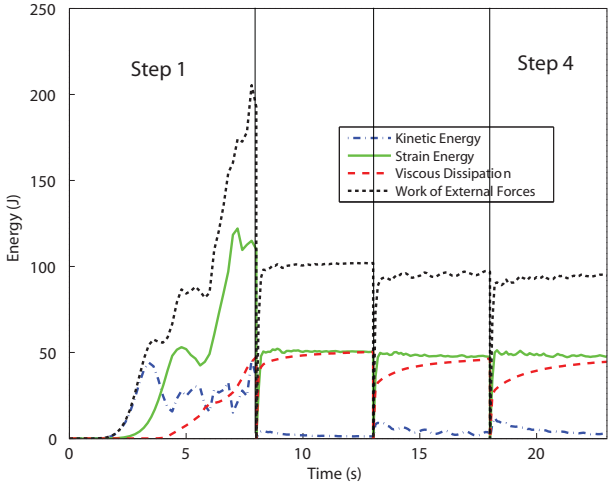

Figure 7. Energy variation for balloon # 1

blue region, and a smaller outward displacement, with $\overline{\Delta r} = +0.0209$ m over the dark red region. The plot of change in azimuth angle, Figure 8(c), shows an approximately linear variation in the circumferential direction, in the range -9 deg to $+6.5$ deg. The jump of 15.5 deg across the cleft indicates that approximately $15.5 \times 200/360 = 8.6$ lobes have been ingested in the cleft.

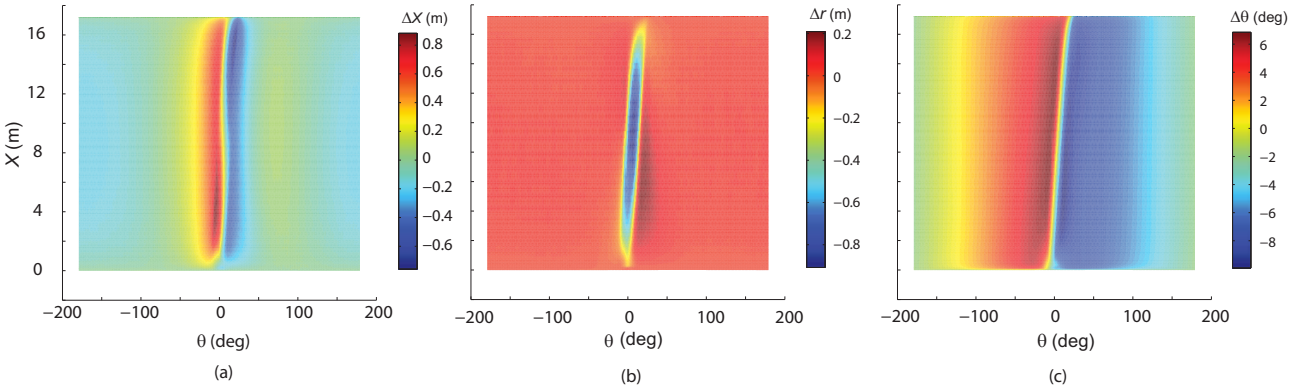

Figure 8. Displacement field in undeformed configuration: (a) Variation of vertical coordinate ΔX; (b) Radius Δr; (c) Azimuth angle $\Delta\theta$.

The film stress distribution at step 1 and step 2 are presented in Figures 9 and 10 respectively. At step 1, a cleft appears as soon as the stress in the bottom region is relaxed and the bottom end fitting is offset from the X-axis. Along the cleft, the film is tensioned in the meridional direction but unstressed in the hoop direction. Once the cleft has formed, the second step resets the bottom constraint to the apex and reapplies the pressure over the whole region. Compared to the axi-symmetric configuration, the height of the clefted balloon is nearly the same but its volume is slightly increased.

A visual comparison, in Figure 11, shows that the simulation result agree remarkably well with the test observation. This it the first time that an S-cleft has been captured computationally.

Of the many factors that may contribute to the formation of S-clefts, it has been conjectured that self-contact within the balloon may play a leading role. We can use our simulation to explore this conjecture and see what happens if the balloon is "magically" allowed to pass through itself. This was investigated by removing the contact option from the simulation.

The results of this modified simulation are presented in Figure 12. This new configuration is still clefted but not in the typically S-shape. Instead of forming an S-cleft, the balloon has formed a meridional cleft

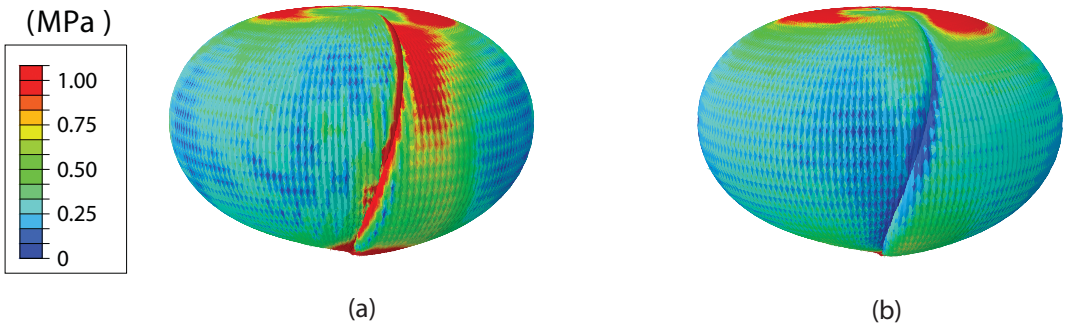

Figure 9. Stress distribution at step 1: (a) Meridional stress; (b) Hoop stress (Units: MPa).

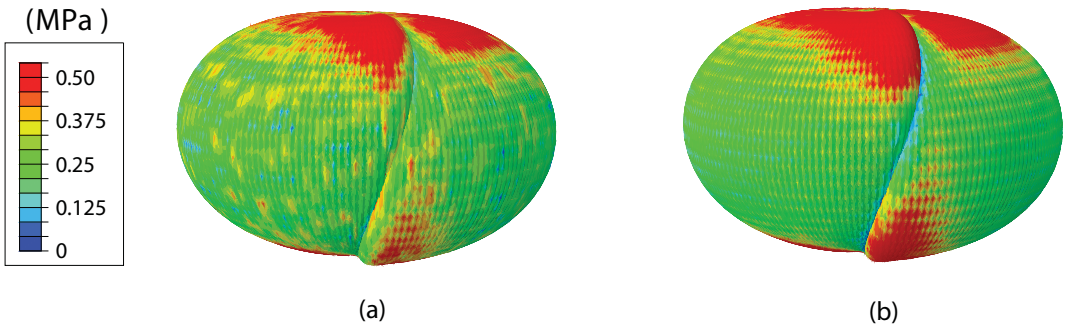

Figure 10. Stress distribution at step 2: (a) Meridional stress; (b) Hoop stress (Units: MPa).

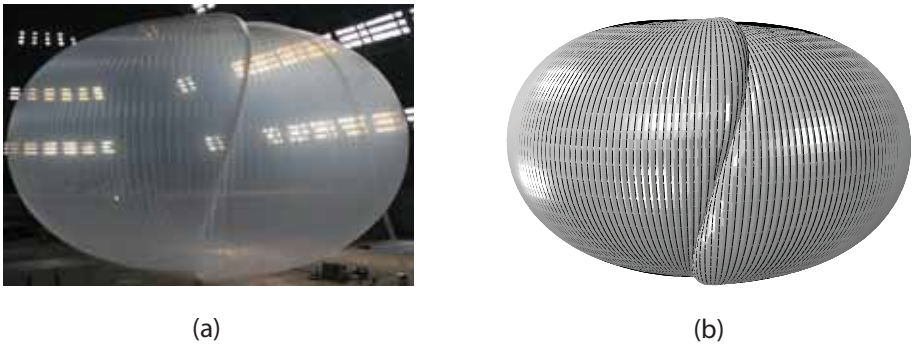

Figure 11. Shape comparison for balloon # 1.

with the spare film arranged around a kind of inner tube attached to the balloon. Severe overclosure of the gap across the contact surfaces has occurred because the membrane has been allowed to penetrate through itself. Compared to the previous analysis, the strain energy of this balloon model is higher.

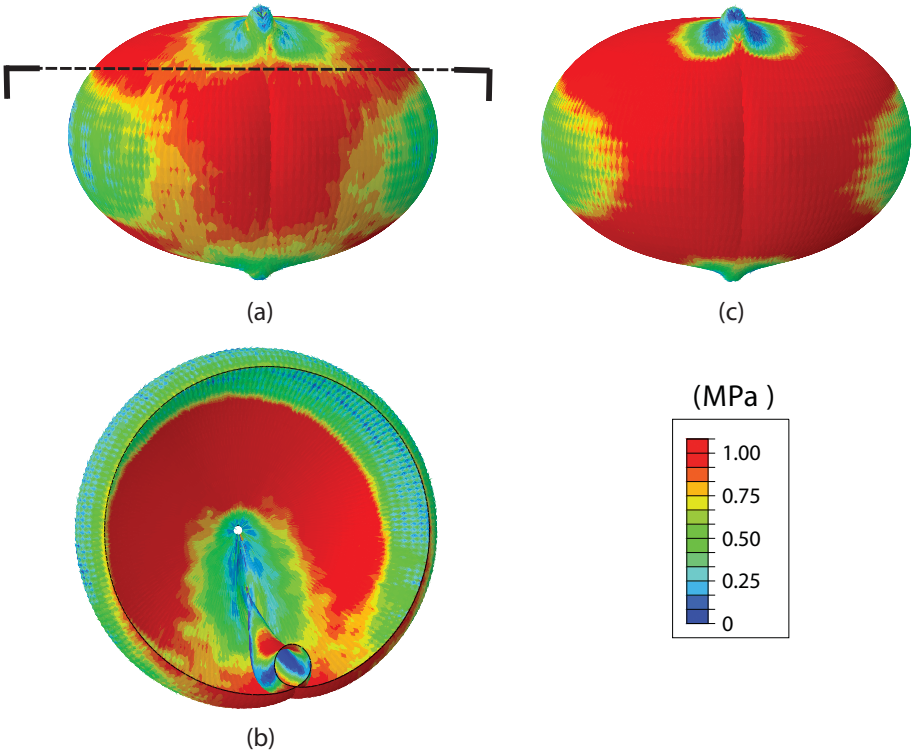

Figure 12. Stress distribution of clefted configuration without contact: (a) Meridional stress; (b) Meridional stress (Cross section); (c) Hoop stress (Units: MPa).

The variation of the total potential energy is a useful tool to study the stability of clefted configurations. Ignoring material dissipation and heat transfer, the variation of total potential energy $\Delta\varepsilon$ is given by

$$\Delta\varepsilon = \Delta\varepsilon_P + \Delta\varepsilon_M \tag{10}$$

where $\Delta\varepsilon_P$ is the variation of the potential energy of the lifting gas, written as $\Delta\varepsilon_P = -\Delta p \Delta V$. $\Delta\varepsilon_M$ is the variation of the strain energy of film and tendons.

The volume of the balloon, V, is defined as the inner space enclosed by the film and is calculated from

$$V = \sum_{i=1}^{m} (\mathrm{Sign}_i \times V_i) - V_{\mathrm{Oc}} \tag{11}$$

Here the summation is the algebraic sum of the volumes of the tetrahedra V_i, where m is the number of triangular elements that model the film. The i-th tetrahedron is constructed as follows: first we pick up a fixed random point (x_0, y_0, z_0) within the enclosed region as the top vertex of the tetrahedron, then we choose the i-th triangular element is its base; the Cartesian coordinates of the three nodes are $(x_{i,1}, y_{i,1}, z_{i,1})$, $(x_{i,2}, y_{i,2}, z_{i,2})$ and $(x_{i,3}, y_{i,3}, z_{i,3})$, see Figure 13. Therefore the volume of this tetrahedron is

$$V_i = \frac{1}{6} \begin{bmatrix} x_0 & y_0 & z_0 & 1 \\ x_{i,1} & y_{i,1} & z_{i,1} & 1 \\ x_{i,2} & y_{i,2} & z_{i,2} & 1 \\ x_{i,3} & y_{i,3} & z_{i,3} & 1 \end{bmatrix}, i = 1, 2...m\cdot \tag{12}$$

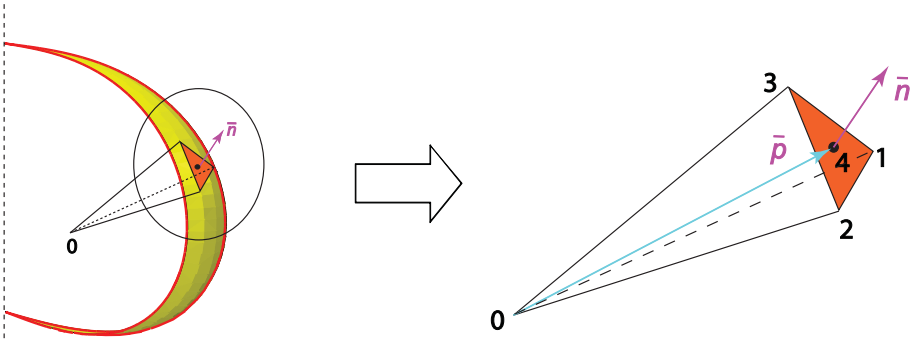

Figure 13. Schematic of volume calculation.

In Figure 13, $\overline{n}$ defines the normal vector to the surface element, and $\overline{p}$ defines the vector pointing from the top vertex O to the centroid of the base 4. Sign_i, the sign of the tetrahedron, is +1 when $\overline{p} \bullet \overline{n} \geq 0$ is satisfied, whereas it is −1 when $\overline{p} \bullet \overline{n} < 0$. Hence, the negative sign applies when the surface is non-convex, e.g., the contact surface is concave. Overclosure occurs in the clefted configuration obtained without a contact model. The volume of the overclosure V_{oc} is the volume of the inner tube in the clefted configuration obtained in this case, and is zero for the other two cases.

Table 4 compares the variation of the total potential energy with reference to the axi-symmetric configuration. $\Delta\varepsilon_P$, i.e. ΔV, is a more significant contributor to $\Delta\varepsilon$ than $\Delta\varepsilon_M$.

If the variation of the potential energy of the lifting gas $\Delta\varepsilon_P$ is neglected, then the principle of minimum strain energy would indicated that the axi-symmetric configuration is the most stable configuration. The clefted configuration ignoring the kinematic constraints imposed by contact gives the minimum total potential energy but this solution is physically infeasible. The clefted configuration obtained by including the contact model has a total potential energy intermediate between the above two models, and hence it is more stable than the axi-symmetric configuration.

Table 4. Variation of total potential energy for balloon # 1

	Strain energy ε_M (J)	Variation of strain energy $\Delta\varepsilon_M$ (J)	Volume V (m^3)	Variation of potential energy of lifting gas $\Delta\varepsilon_P$ (J)	Variation of total potential energy $\Delta\varepsilon$ (J)
Axi-symmetric config.	45.84	0	6876	0	0
Clefted config. (with contact)	48.45	2.61	6939	-711.9	-709.3
Clefted config. (without contact)	75.15	29.31	7195	-3604.7	-3575.4

Next, we use the simulation to answer the following question of great practical importance. Does the cleft disappear if we significantly increase the base pressure? We have computed the equilibrium shape for $p_D \rightarrow 100$ Pa while keeping the pressure gradient constant and the results are shown in Figure 14. The stress levels are higher but, instead of unfolding the S-cleft has moved inwards and the indentation has becomes even deeper. Recall that the total volume V was 6939 m^3 at Δp_D=10 Pa, and it increases to 7448 m^3 at Δp_D=100 Pa. Also, the total potential energy ε has decreased, which indicates that this more highly pressurized configuration is even more stable. This result shows the irreversibility of the S-cleft by applying a higher pressure.

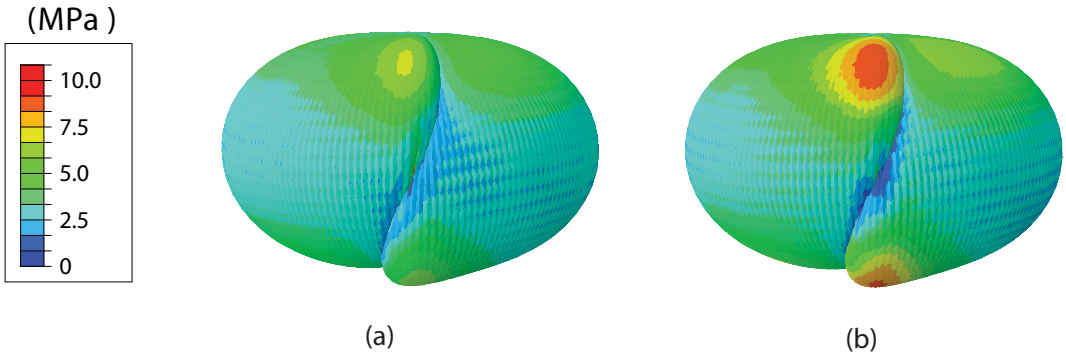

Figure 14. Stress distribution at Δp_D=100 Pa: (a) Meridional stress; (b) Hoop stress (Units: MPa).

Table 5. Constraint shift simulation steps for balloon # 4

Step		Loading time (s)	Viscosity coefficient
Step No.	Substep No.		
1	1	10.0	0.8
2	2	5.0	0.8
	3	5.0	0.2
	4	5.0	0.05
	5	5.0	0.02
	6	5.0	0.02
	7	5.0	0.01
	8	5.0	0.01

VI. Results for Balloon # 4 with 55° Bulge Angle

The analysis for this balloon followed exactly the same steps described in Section V and the simulation steps are presented in Table 5. Complete deployment of this balloon had been observed during the indoor test. Considering that no clefts existed in the final configuration, a much smaller viscosity coefficient was applied to achieve the greatest possible stability in the simulations. Hence, see Figure 15, more substeps were required to achieve full convergence at the end of the simulation. The large oscillations in the kinetic energy decreased throughout the substeps of step 2.

In Figure 16, note that after the constraint shift in step 1, the stress distribution becomes quite asymmetric and the balloon takes up a clefted configuration. The shape at the end of step 2 is nearly axi-symmetric with only a small change of stress in a small region near the bottom apex, as shown in Figure 17.

Figure 18 provides a visual comparison between the simulation result and the test. They generally agree well: no cleft was observed in the experiment, whereas the simulation shows a deployed shape with only a tiny residual distortion.

Again we removed the general contact from the original model and obtained the stress distribution shown in Figure 19. Compared to the corresponding results for the original model, we have complete deployment in both cases, but the new model without contact shows a bit more residual distortion. Table 6 confirms the similarity of their shapes by the very close values of the enclosed volumes. The small variation of total potential energy between the results for the two models, also shown in Table 6, proves that the 55 degree bulge angle balloon will achieve an axi-symmetric configuration after pressurization.

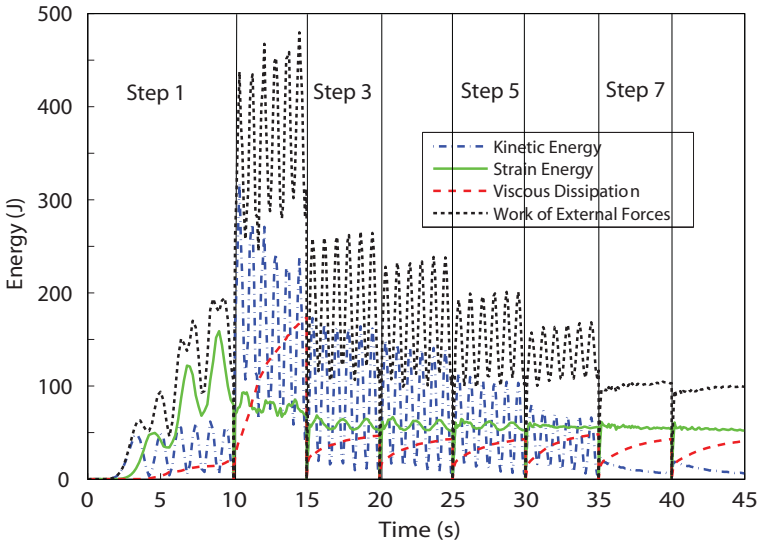

Figure 15. Energy variation for balloon # 4

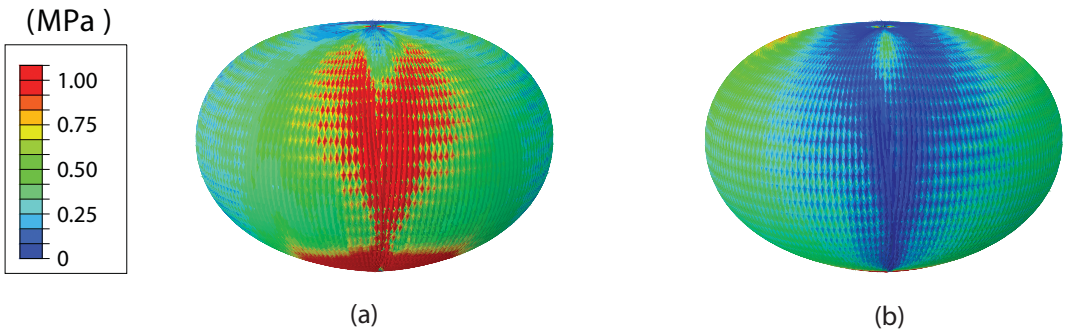

Figure 16. Stress distribution of balloon # 4 at step 1: (a) Meridional stress; (b) Hoop stress (Units: MPa).

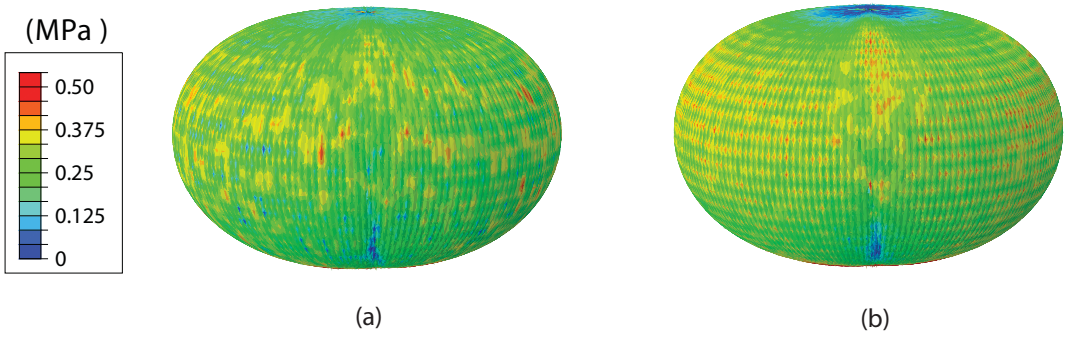

Figure 17. Stress distribution of balloon # 4 at step 2: (a) Meridional stress; (b) Hoop stress (Units: MPa).

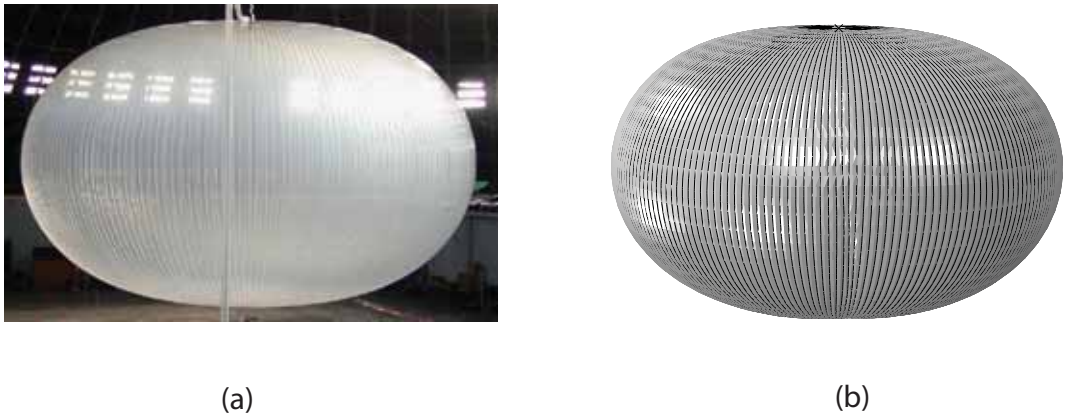

Figure 18. Shape comparisons of balloon # 4.

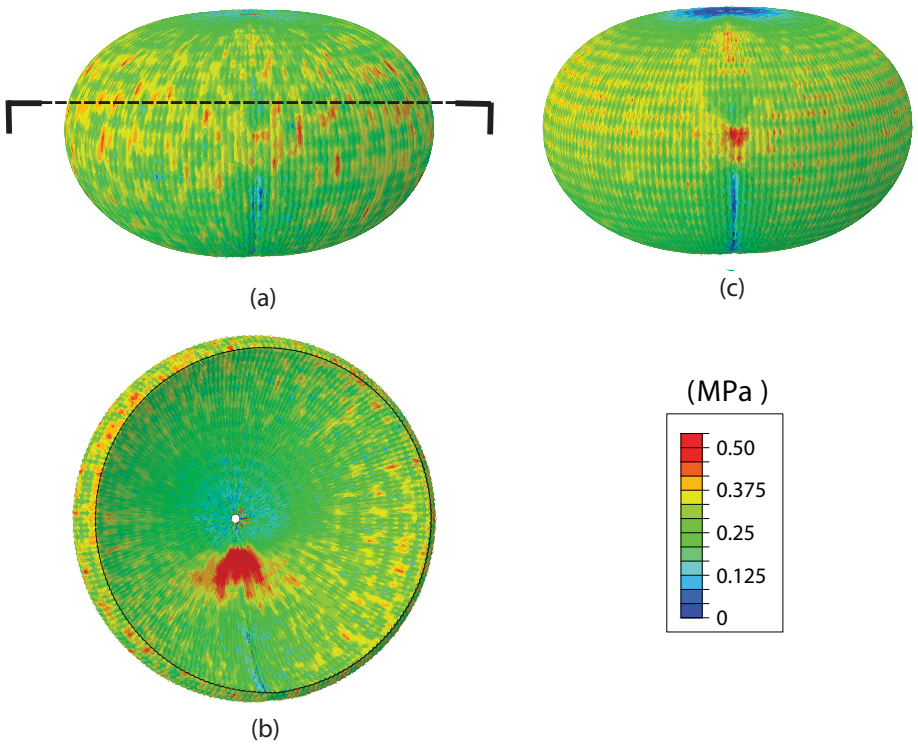

Figure 19. Stress distribution of balloon # 4 without contact: (a) Meridional stress; (b) Meridional stress (Cross section); (c) Hoop stress (Units: MPa).

Table 6. Variation of total potential energy of balloon # 4

	Strain energy ε_M (J)	Variation of strain energy $\Delta\varepsilon_M$ (J)	Volume V (m^3)	Variation of potential energy of lifting gas $\Delta\varepsilon_P$ (J)	Variation of total potential energy $\Delta\varepsilon$ (J)
Axi-symmetric config.	50.78	0	7239.7	0	0
Unclefted config. (with contact)	52.18	1.4	7240.3	-6.78	-5.38
Unclefted config. (without contact)	52.71	1.93	7246.3	-74.58	-72.65

Table 7. Constraint shift simulation steps for balloon # 5

Step		Loading time (s)	Viscosity coefficient
Step No.	Substep No.		
1	1	10.0	0.8
2	2	5.0	0.8
	3	5.0	0.4
	4	5.0	0.2
	5	5.0	0.1
	6	5.0	0.05
	7	5.0	0.02
	8	5.0	0.01

VII. Results for Balloon# 5 with 90° Bulge Angle

In this section we investigate a third balloon that, although very close in design to Balloon #1, was actually sufficiently different that when it was tested it took up an axi-symmetric configuration after full pressurization. Therefore this balloon provides a very good test for our clefting test. We follow the same loading procedures as before and the two-step simulation are presented in Table 7. The energy variation is shown in Figure 20.

The symmetric stress distribution is broken in step 1, in Figure 21, and its symmetry is finally recovered in Figure 22 at the end of step 2 except for a small distortion near the bottom apex.

In Figures 23 the simulation result is visually compared with the test observation. They are consistent in predicting the completely deployed shape except for a small residual distortion shown in the simulation picture.

Repeating the analysis after removing the general contact definition from the model leads to the clefted configuration in Figure 24: overclosure can be seen in the cross section of the balloon, in contrast to the full deployment of the original model. Comparison of the variation of total potential energy, Table 8, reveals that contact plays a key role in producing the cleft: on the one hand, addition of general contact will increase the total potential energy; on the other hand, it helps to prevent clefting.

VIII. Discussion and Conclusion

The objective of this study was to develop a technique to predict clefting in lobed super-pressure balloons. A perturbation method to artificially break the symmetry of a balloon and seeding a clefting perturbation has been presented. Gravity effects, isotropic wrinkling of the film and frictionless self-contact in the balloon

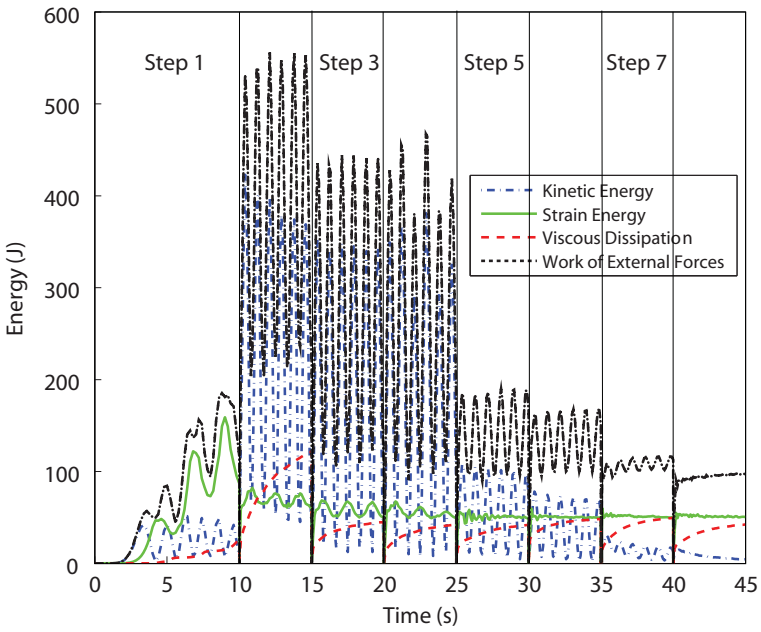

Figure 20. Energy variation of balloon # 5

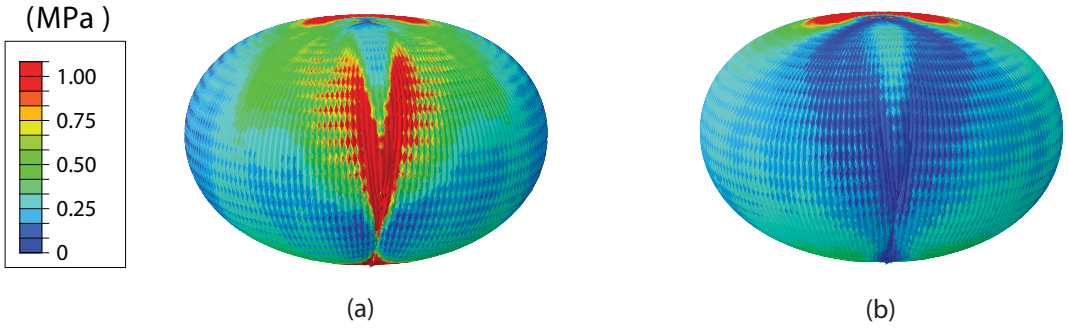

Figure 21. Stress distribution of balloon # 5 at step 1: (a) Meridional stress; (b) Hoop stress (Units: MPa).

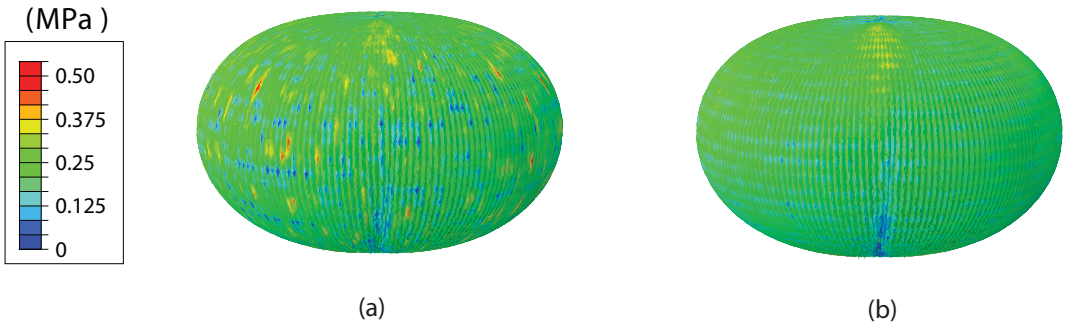

Figure 22. Stress distribution of balloon # 5 at step 2: (a) Meridional stress; (b) Hoop stress (Units: MPa).

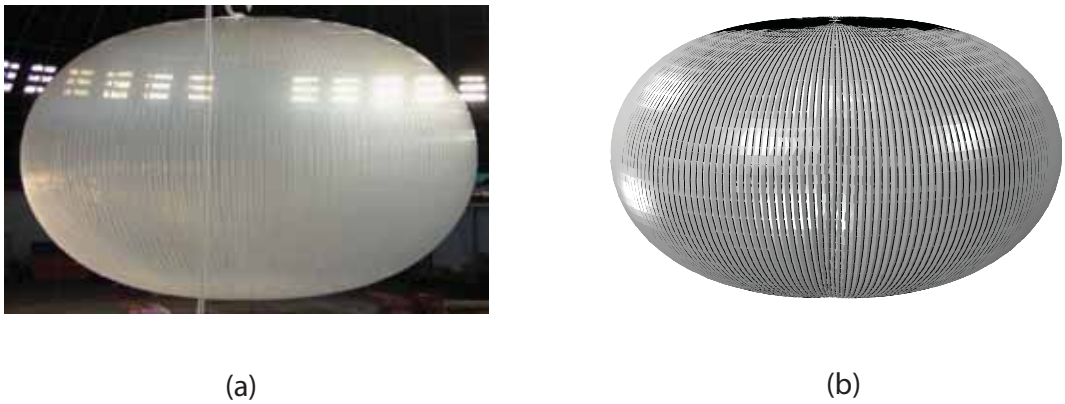

Figure 23. Shape comparisons of balloon # 5.

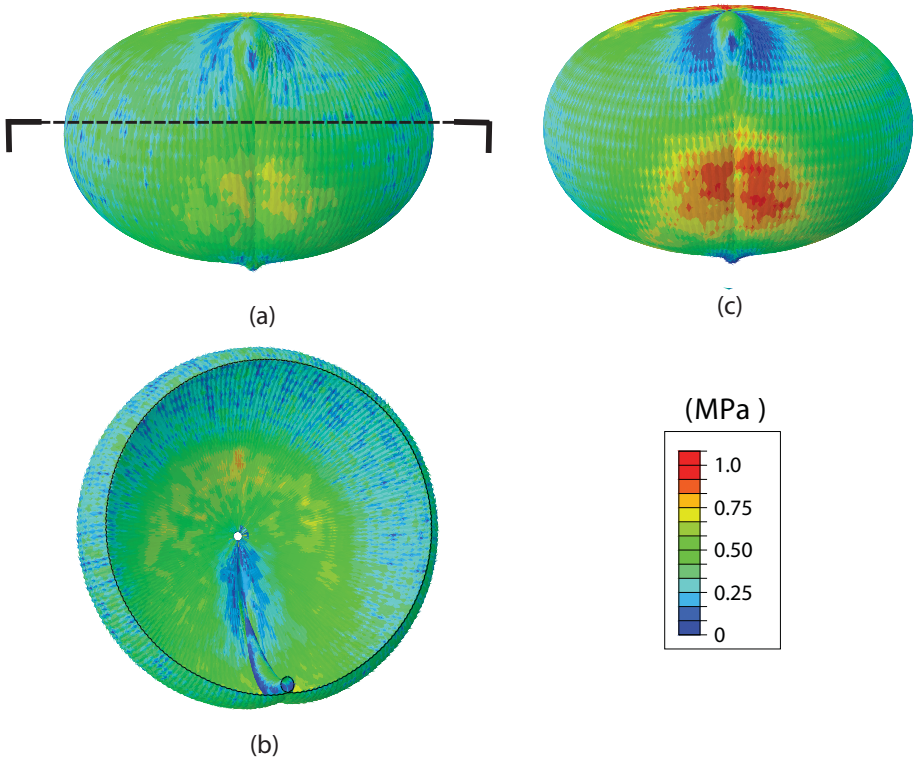

Figure 24. Stress distribution of balloon # 5 without contact: (a) Meridional stress; (b) Meridional stress (cross section); (c) Hoop stress (Units: MPa).

Table 8. Variation of total potential energy of balloon # 5

	Strain energy ε_M (J)	Variation of strain energy $\Delta\varepsilon_M$ (J)	Volume V (m^3)	Variation of potential energy of the lifting gas $\Delta\varepsilon_P$ (J)	Variation of total potential energy $\Delta\varepsilon$ (J)
Axi-symmetric config.	48.33	0	7138	0	0
Unclefed config. (with contact)	50.28	1.95	7145	-79.81	-77.1
Clefed config. (without contact)	54.29	5.96	7278	-1582	-1576

are all included in the analysis. The method has been shown to be an effective way of both capturing S-clefts and predicting clefting in balloons with different cutting pattern designs.

Seeding a clefting perturbation is the key step in our analysis; it has been implemented through the constraint-shift method, which has been divided into two steps. Starting from the cyclically symmetrical configuration of the balloon, in step 1, the balloon is constrained at a single offset point and the pressure is removed in the bottom region, below the shifted constraint. Thus the stress distribution becomes asymmetric and a single large cleft is allowed to appear. Once this disturbance has been introduced, in step 2 of the analysis the bottom apex constraint is moved back to the original apex and the non-uniform pressure is applied to the whole balloon.

The constraint-shift method has been tested on three 27 m diameter super-pressure balloons that had been designed and tested by the NASA super-pressure balloon team, Balloon # 1, # 4 and # 5. These balloons all had 200 lobes but the lobe bulge angles at the equator were respectively 98.1 °, 55 ° and 90 °. In the indoor tests Balloon # 1 had remained clefted, with a typical S-cleft at a pressure of 10 Pa, while the other two balloons had deployed completely.

Visual comparison between simulation results and test observations for the shape of the S-cleft occurring in Balloon # 1 have shown remarkable agreement and so it can be concluded that for the first time an S-cleft has been captured computationally. We have computed the total potential energy of this balloon in the clefted configuration and compared it to the energy in the axi-symmetric configuration; because the volume of the clefted balloon is larger, we have found that the clefted shape is more stable. Hence increasing the pressure in this balloon will not eliminate the cleft. We have also shown that the S-cleft will not disappear if the balloon is allowed to pass through itself. Instead of forming an S-cleft, the balloon formed a meridional cleft with the spare film arranged around a kind of inner tube attached to the balloon.

The constraint-shift method has also successfully predicted the full deployment of Balloons # 4 and # 5.

Acknowledgments

We thank the NASA Super-Pressure Balloon Team for their contributions to this research and in particular Henry Cathey for kindly providing test data and Rodger Farley, Jim Rand and David Wakefield for helpful discussions. We are grateful to Chris Calladine for helpful suggestions. This research was supported by the NASA Balloon Program Office (contract monitor Danny Ball).

References

[1]Cathey, H. M., "ULDB 27 m diameter balloon indoor launch, inflation, and deployment test report," Test report, Physical Science Laboratory, NASA BPO, May 2007.

[2]Calladine, C.R. Stability of the Endeavour balloon, Buckling of Structures. In: I. Elishakoff, J. Arbocz, C.D. Babcock, and A. Libai, eds., Elsevier Science Publishers, 133-149 (1988).

[3]Lennon, B.A., and Pellegrino S. Stability of lobed inflatable structures, 41st AIAA/ASME/ASCE/AHS/ASC SDM Conference, AIAA 2000-1728 (2000).

[4]Baginski, F. and Collier, W., "Energy minimizing shapes of patially inflated large scientific baloons," *Advances in Space Research*, **21**, 975–978, 1998.

[5]F. Baginski, Q. C. and Waldman, I., "Designing the shape of a large scientific balloon," *Appplied Mathematical Modeling*, **25**, 953–966, 2001.

[6]Baginski, F., "A mathematical model for a partially inflated balloon with periodic lobes," *Advances in Space Research*, **30**, 1167–1171, 2002.

[7]Pagitz, M. and Pellegrino, S., "Buckling pressure of "pumpkin" balloons", *International Journal of Solids and Structures* **44**, 6963-6986, 2007.

[8]Xu, Y., *A Computational Study of Lobed Balloons*, Ph.D. thesis, Department of Engineering, University of Cambridge, 2007.

[9]Baginski, F. and Brakke, K., "Exploring the Stability Lanscape of Constant-Stress Pumpkin Balloon Designs," *Journal of Aircraft*, **47**, 849–857, 2010.

[10]Deng, X. and S. Pellegrino, Computation of partially inflated shapes of stratospheric balloon structures, *48th AIAA/ASME/ASCE/AHS/ASC Structures, Structural Dynamics and Materials Conference*, 7-10 April 2008, Schaumburg, Illinois, AIAA-2008-2133.

[11]Deng, X. and Pellegrino, S., "Finite element simulations of clefting in lobed super-pressure balloons," *AIAA Balloon Systems Conference*, 4-7 May 2009, Seattle, Washington, AIAA-2009-2816.

[12]Taylor, G.I., On the shapes of parachutes. From: *The Scientific Papers of Sir G.I. Taylor*, edited by G.K. Batchelor, Cambridge University Press, **3**, 26-37 (1963).

[13]Mladenov, I. M., and Oprea J.. The Mylar balloon revisited, *American Mathematical Monthly*, **110**, 761-784 (2003).

[14]Miller, R. K. and Hedgepeth, J. M., "An Algorithm for Finite Element Analysis of Partly Wrinkled Membranes," *AIAA Journal*, Vol. 20, Dec. 1982, pp. 1761–1763.

[15]Adler, A. L., *Finite element approaches for static and dynamic analysis of partially wrinkled membrane structures*, Ph.D. thesis, University of Colorado at Boulder, 2000.

[16]Lennon, B. A., *Equilibrium and Stability of Inflatable Membrane Structures*, Ph.D. thesis, Department of Engineering, University of Cambridge, 2002.

[17]Deng, X. and S. Pellegrino, Wrinkling of orthotropic viscoelastic membranes, *51th AIAA/ASME/ASCE/AHS/ASC Structures, Structural Dynamics and Materials Conference*, 12-15 April 2010, Orlando, FL, AIAA-2010-2606.